ORIGINAL ARTICLE

An improved cable-cylinder bracing system with quarter-ring yielding devices for seismic retrofit of steel moment frames

Oreste S. Bursi[1] · **Nader Fanaie**[2] · **Shervin Safaei Faegh**[2] ·
Omid Sepasgozar Sarkhosh[3]

Abstract

This study proposes an innovative hybrid lateral load-resisting system, termed the ring-cable-cylinder bracing system, aimed at improving the energy dissipation capacity and ductility of the previously introduced cable-cylinder bracing (which offers relatively the same level of seismic energy dissipation and ductility as the original bare steel frame), and minimizing the damage to the beam-to-column connections via utilizing quarter-ring curved yielding devices. First, the proposed bracing system and its working mechanism are introduced. A mathematical procedure based on the theorem of the least work and the method of virtual work is then presented to derive highly-accurate, practical, and easy-to-use equations for calculating the thickness of the utilized quarter-ring yielding devices. The design requirements for these curved devices, based on the characteristics of the frame in which they are utilized, are also discussed exhaustively. In the next step, the presented formulae's accuracy and usability are comprehensively investigated by conducting a finite element parametric study. The results show that the proposed system can provide an extra source of energy dissipation and ductility. It was also observed that the new system leads to an increase in both initial stiffness and ultimate strength and limits the pinching phenomena in the hysteretic cycles.

Keywords Quarter-ring device · Cable-cylinder bracing system · Method of least work · Low-yield-point steel · Failure mechanism-based analysis · FE model

✉ Nader Fanaie
  fanaie@kntu.ac.ir

  Oreste S. Bursi
  oreste.bursi@unitn.it

  Shervin Safaei Faegh
  safaei.faegh.s@gmail.com

  Omid Sepasgozar Sarkhosh
  omid.sepasgozar@gmail.com

[1] Department of Civil, Environmental and Mechanical Engineering, University of Trento, Trento, Italy

[2] Faculty of Civil Engineering, Department of Civil Engineering, K. N. Toosi University of Technology, No. 1346, Valiasr St, PO Box, 15875-4416 Tehran, Iran

[3] Faculty of Engineering, Department of Civil Engineering, University of Guilan, Rasht, Iran

1 Introduction

Steel moment frames are typically designed to act as ductile lateral load-resisting structural systems that dissipate seismic energy through large plastic deformations. Nonetheless, extremely severe earthquakes have been observed to induce unacceptably large amounts of story drift in these systems, leading to heavy structural damage. To address this issue, researchers have proposed different methods for seismic retrofit of existing buildings and safer design of new structures.

Among the proposed methods, many focused on new types of bracing systems with innovative elements. In particular, Hou and Tagawa's 2009 paper proposed using a pair of cables in combination with a hollow cylindrical member as a new bracing method for seismic strengthening of steel moment frames. In this system, depicted in Fig. 1, the two bracing cables are bundled at their intersection point by a central cylinder made of either high-stiffness steel or low-stiffness PVC pipe. The utilization of the central cylinder in this system requires longer cables than those in an ordinary cross-cable bracing system. If the cylinder is made of a high-stiffness material, it works as a relatively rigid component that undergoes nearly zero deformation. As a result, the cables' lengths do not remain constant during the lateral displacement of the frame, and thus the bracing system starts acting immediately as the seismic loads from an earthquake begin to affect the structure.

The deformed shape of a frame with the abovementioned cable-cylinder bracing system with a high-stiffness cylinder is shown in Fig. 1(b). When the frame is subjected to the rightward static lateral displacement δ, the center of the cylinder first moves horizontally towards the right by $\delta/2$, and then rotates counterclockwise by $\theta°$ to neutralize the moment caused by the cables. Figure 2 shows the tensile forces induced in the cable bracing members as the frame deforms. As shown in this figure, the rotation of the cylinder causes both cables to be in tension; Thus, the tensile force T_b is induced member b in addition to the one in member a (T_a).

The cable-cylinder bracing system mentioned above, while requiring frame members with smaller cross-sectional areas, offers many advantages such as drastically reduced story drift, less compressive force in the columns, and the same seismic energy dissipation capacity and ductility compared to the original bare steel frame (Hou and Tagawa 2009; Fanaie et al. 2016). Also, since both of the cables remain in tension during the lateral
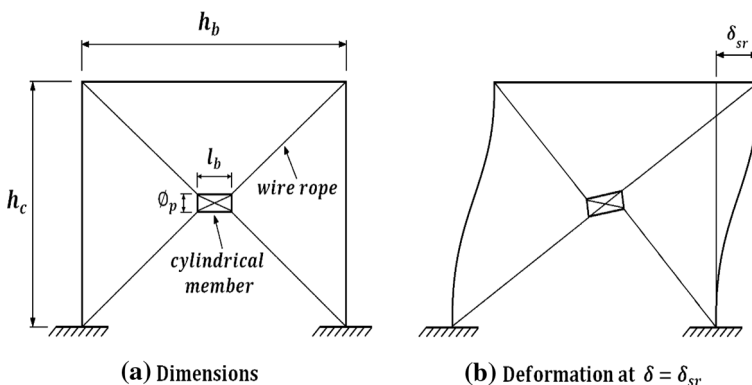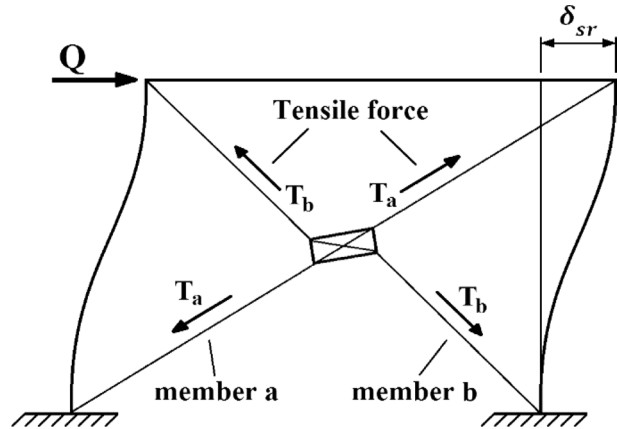

Fig. 1 The cable-cylinder bracing system proposed by Hou and Tagawa (2009) **a** Geometric details **b** Deformed frame in case of a high-stiffness cylinder

Fig. 2 Tensile forces in the cable-cylinder bracing system with a high-stiffness cylinder

displacement of the frame, the undesirable effects induced by the loosening of the cables in the ordinary cross-cable system are eliminated. The cable cable-cylinder bracing system also prevents the concentration of damage in a specific story, also known as the soft story effect.

Several other studies have also proposed innovative solutions for improved seismic energy dissipation in moment frames utilizing different types of annular and curved elements, such as ring-shaped and U-shaped components. Beheshti-Aval et al.'s (2013) study introduced a new hybrid friction/hysteretic damper system for steel frames with concentric bracing to improve seismic energy dissipation. This hybrid system, illustrated in Fig. 3, includes a circular ring-shaped steel yielding element connected to the bracing elements via slotted-bolted connections that act as friction devices.

Deng et al. (2013) developed and examined a novel crawler steel damper consisting of two U-shaped steel energy dissipation plates coupled via two connection plates. In this system, the two U-shaped steel plates, which are bolted to the upper and lower connection plates, dissipate energy through plastic deformations.

Maleki and Mahjoubi (2013) proposed a new passive earthquake energy dissipative device termed the dual-pipe damper (DPD). The proposed device includes two pipes

Fig. 3 The hybrid friction/hysteretic damper system with a circular ring-shaped yielding element in a concentrically-braced frame (Beheshti-Aval et al. 2013)
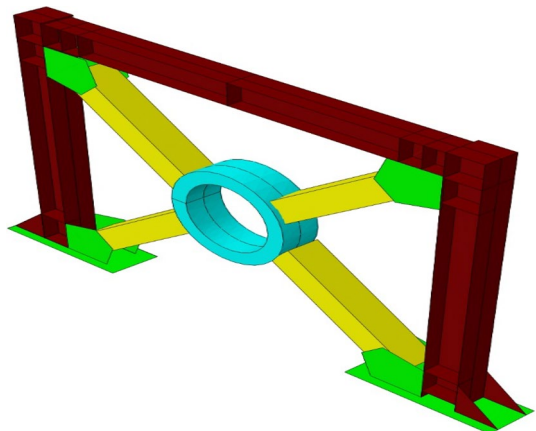
welded at designated locations and dissipates the input energy mainly through inelastic cyclic deformations. In this experimental study, all four samples of DPD exhibited excellent ductility and energy dissipation, as well as stable hysteresis loops.

Andalib et al. (2014) presented an experimental investigation of a steel ring device comprised of two steel half-ring plates meant to be used as an energy dissipator component in bracing systems. This proposed ring-shaped energy dissipation device is connected to the bracing elements in the corresponding frame using bolted connections rather than welded ones, which offers advantages such as easy installation and replacement. Their experimental results showed that the proposed ring device exhibits a high energy dissipation level by behaving like a fuse in the structural system and postpones buckling in bracing members.

Utomo et al. (2015) carried out a finite element study on an innovative vertical steel pipe device strengthened by two trapezoidal plates attached to the outside of the pipe and three inner rings. The rings were designed not to yield; however, the pipe and trapezoidal plates were designed to yield and hence provide an appropriate amount of energy dissipation. The proposed pipe device experienced a substantial amount of cyclic yielding under the loading applied.

Hsu and Halim (2017) proposed and experimentally tested a novel steel curved damper design suitable for seismic strengthening or retrofitting of structures. In their study, a set of cyclic loading tests were conducted on three types of structures: a semi-rigid frame, a rigid frame, and a pinned frame equipped with different curved damper placements. They concluded that the proposed curved dampers have stable hysteretic behavior under compression and tension loading and could lead to substantial improvements in strength, stiffness, and energy dissipation when utilized in moment-resisting steel frames.

Zahrai and Hosein Mortezagholi (2017) investigated the cyclic performance of elliptical dampers with shear diaphragms in steel frames equipped with the Chevron bracing system. They also presented the relationships for the optimum design of such devices. Their results showed that in addition to significant contributions to energy dissipation, such devices act like fuses and prevent the braces' buckling and yielding.

Cheraghi and Zahrai (2017) conducted an experimental investigation of the performance of multi-level pipe in pipe dampers. These dampers consist of nested pipe segments, which allow for variable dynamic response parameters such as stiffness, strength, and damping ratio at different earthquake intensities. The samples exhibited suitable seismic energy absorption and ductility and had stable hysteresis curves.

Xie et al.'s (2018) suggested a simplified analytical model for simulating the hysteretic behavior of U-shaped steel dampers with horizontal bidirectional steel deformation. This model, known as the modified multiple shear spring model, is comprised of a set of shear springs with different nonlinear specifications in a radial configuration. Their results showed that the model is able to offer a sufficient level of accuracy to simulate hysteretic behavior of U-shaped steel damper, providing a practical and improved method for assessment of such devices through seismic response analysis.

Henriques et al.'s (2019) research proposed an innovative dissipative connection design for braced frames. This design consists of a steel plate bent to a U shape that connects a given brace to its adjacent column in a steel frame. The obtained results proved that the proposed connection is an efficient option for dissipating input seismic energy through inelastic deformations in braced steel frames.

By conducting experimental and numerical studies, Taiyari et al. (2019) introduced a new bracing system comprised of U-shaped elements intended as a hysteretic device for seismic energy dissipation. Their results confirmed that the proposed system has a high energy dissipation capacity and stable hysteretic behavior.

Another experimental study conducted by Chen et al. (2019) designed a new graded yield metal damper composed of two annular metal components. The system consists of inner and outer ring-shaped metal devices of two different sizes, connected via middle steel plates using bolts, as depicted in Fig. 4. The obtained experimental results indicated that these ring-shaped metal devices exhibit remarkable deformation and energy-dissipation capacities as well as a considerable anti-fatigue performance.

It should be noted that the designs proposed for the utilization of curved steel devices have not been limited to only steel structures. Chen et al.'s (2020), for example, studied the idea of using curved quarter-ring steel braces to improve the performance of post-tensioned precast reinforced concrete (RC) beam-to-column joints. The results showed that the proposed curved braces provide suitable strength, stiffness, and seismic energy dissipation, confirming such devices' practicality and feasibility in post-tensioned RC structures.

In addition to the abovementioned studies, several other research papers, such as those by Chen and Jhang (2011) and Zhang et al. (2013), have focused on utilizing structural fuses equipped with low-yield-point (LYP) steel plates installed adjacent to the main members to minimize the damage inflicted by earthquakes. LYP steel plates could be used as suitable alternatives to conventional ones towards improving structural systems' performance as they exhibit superior deformation capacity. Besides, utilizing LYP steel devices allows for reducing the compactness ratio of the corresponding element, which, in turn, decreases the risk of local buckling.

In an ordinary cable-cylinder bracing system such as the one proposed by Hou and Tagawa (2009), both of the cross-cables passing through the stiff central cylinder are designed to remain elastic as the steel frame is subjected to lateral loads. Hence, this bracing system offers a relatively the same level of seismic energy dissipation capacity and ductility as the original bare frame. Consequently, in a steel frame with the ordinary cable-cylinder bracing system, the structure's energy dissipation and ductility are almost entirely provided by the formation of plastic hinges at the beams' ends near the beam-to-column connections, with a rather insignificant contribution from the bracing system. Therefore, there still seems to be a need for an improved and modified bracing system for seismic retrofit of defective steel frames capable of better contributing to the structure's energy dissipation and ductility capacities and decreasing the damages inflicted upon important structural components such as panel zones and beam-to-column connections in the event of strong earthquakes.

This study proposes an innovative hybrid lateral load-resisting system that can be used either as an independent lateral load-resisting system or in seismic retrofit of steel moment frames, termed the ring-cable-cylinder bracing system, aimed at improving the energy dissipation capacity and ductility of the previously introduced cable-cylinder bracing and deviating the damage from beam-to-column connections and concentrating failure

Fig. 4 Configuration of the graded yield metal damper proposed by Chen et al. (2019)
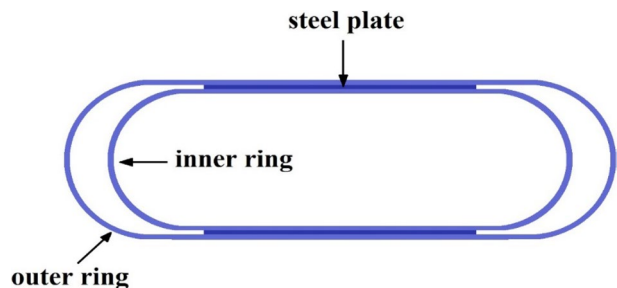
on quarter-ring curved yielding devices. First, the proposed bracing system and its working mechanism are introduced. A mathematical procedure based on the theorem of the least work and the method of virtual work is then presented to derive highly-accurate, practical, and easy-to-use equations for calculating the thickness of the utilized quarter-ring yielding devices. The design requirements for these curved devices, based on the characteristics of the frame in which they are utilized, are also discussed exhaustively. In the next step, the presented formulae's accuracy and usability are comprehensively investigated by conducting a finite element parametric study. Ultimately, the advantages and improvements offered by the proposed system are assessed in detail by adding a set of the devised quarter-ring yielding devices to the verified finite element model of a previously tested steel frame with cable-cylinder bracing.

2 Utilization of quarter-ring yielding devices in the cable-cylinder bracing system

As discussed in the previous section, the cables in an ordinary cable-cylinder bracing system are designed to remain in the elastic range, and hence, such a lateral-load resisting system offers a limited contribution to the structure's energy dissipation and ductility capacities. To improve the performance of the ordinary cable-cylinder bracing, in this research, it is proposed that four curved yielding devices, in the shape of quarter-rings, be utilized to connect the cross-cables to the beam-to-column connections, as illustrated in Fig. 5. The resulting hybrid bracing system can improve the seismic performance of steel frames by
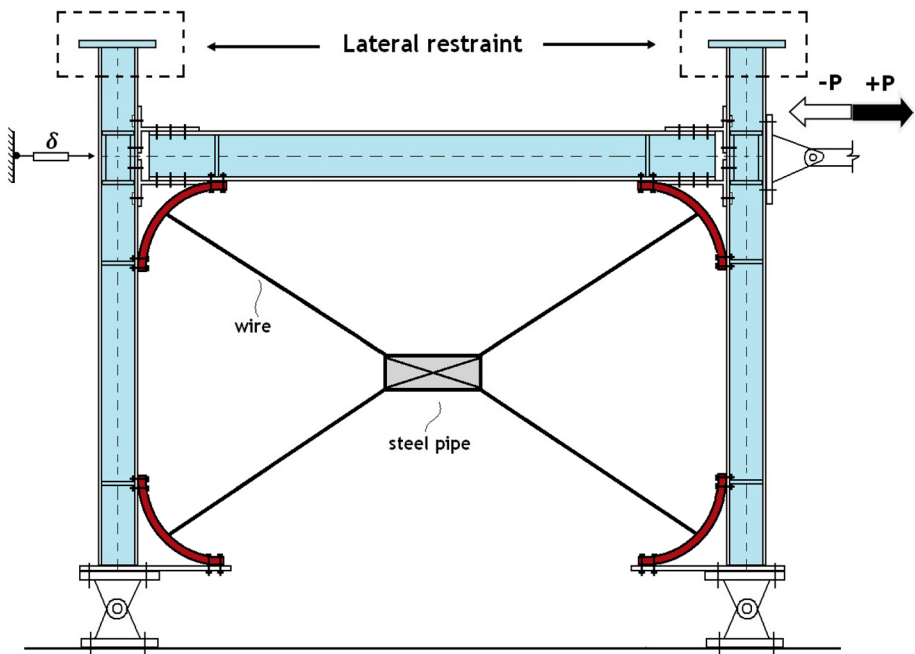

Fig. 5 Schematic illustration of the proposed ring-cable-cylinder bracing system

having extra sources in energy dissipation and providing increased ductility through the early-stage yielding of the suggested quarter-ring devices. Accordingly, this proposed system can effectively protect the beam-to-column connections from sustaining severe damage during strong earthquakes and mitigate and also divert the destructive effects of wire ropes on beam-to-column connections observed in ordinary cable bracing systems.

Since the beams and columns are perpendicular to each other in a typical steel frame, the angle of the curvature for the yielding devices should be 90° for an easy installation. Thus, these quarter-ring components can be produced by dividing a steel pipe into four equal segments or cutting and forming a flat steel plate.

As the lateral load is exerted on a steel frame with the ring-cable-cylinder bracing system, each quarter-ring device is subjected to a concentrated force from the cable connected to it, which causes bending moment as well as axial and shear forces in these curved components. Consequently, the drastic tensile forces in the bracing cross-cables generated by a severe earthquake result in the formation of numerous plastic hinges in the quarter-ring yielding devices. Hence, these devices act as additional means of energy dissipation and sources of ductility within the structure.

Considering the working mechanism of the proposed ring-cable-cylinder bracing system discussed above, it is recommended that low-yield-point (LYP) steel be used for fabricating the quarter-ring yielding devices in this system to achieve a better and more stable cyclic behavior. LYP steel has a relatively lower yield point compared to conventional constructional steel. Its superior plastic deformation capacity allows the proposed quarter-ring devices to enter the plastic range earlier and continue functioning while undergoing large deformations. Thus, using LYP steel rather than conventional constructional steel can elevate the energy dissipation and ductility capacity of the quarter-ring hysteretic devices and hence improve the cyclic performance of the proposed ring-cable-cylinder bracing system.

The tensile forces in the two cross-cables and the curvature of the quarter-ring devices allow for arch action in these elements, which gives additional stiffness to the frame and thus enhances the structure's stability in the event of a strong earthquake. Thus, improved frame stability could be noted as another advantage of utilizing the curved yielding devices in the proposed ring-cable-cylinder bracing system. Besides, as each quarter-ring device is connected to the frame by four bolts (two for connecting to the beam flange and two for connecting to the column flange), they can be easily replaced with new ones if other elements would remain intact after a severe earthquake, which could also be counted as a benefit of the proposed bracing system.

3 Analysis of the proposed quarter-ring curved devices with the method of least work

Because of the particular geometry and curvature of the proposed quarter-ring devices, their bolted connections to the beams and columns of the frame can be considered as rigid connections with an adequate approximation level. Therefore, each of these devices could be analyzed as a distinct fixed-end curved element with the radius of curvature R, as displayed in Fig. 6. Accordingly, when the tensile force in the bracing cable becomes large enough during a strong earthquake, it leads to the formation of two plastic hinges at the curved element's fixed supports and one in the middle of the curved element, where it is applied to the quarter-ring device as the concentrated force

Fig. 6 The quarter-ring device considered as a curved element with two fixed supports subjected to the concentrated tensile force *F*
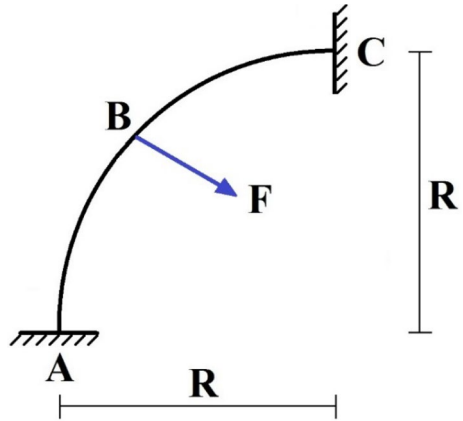
F. These three plastic hinges dissipate the input seismic energy during a severe earthquake and increase the steel frame's ductility capacity.

The angle at which the tensile force is exerted on the curved element depends on the beam length, column height, and the central cylinder's internal diameter and length. In each desired frame, it is easily possible to adjust the cables' angles to 45° (in the radial direction of the curved element), as depicted in Fig. 7, by doing a trial and error process through selecting different values for the length and internal diameter of the central cylinder.

In the case where the cable is not configured in a radial direction, its tensile force could be resolved into two components with radial and tangential directions. The tangential component is then considered as an anti-symmetric loading for the curved device. Based on the properties of symmetric structures subjected to anti-symmetric loading, this anti-symmetric loading does not induce any bending moment in the middle of the curved element. It should be noted that the axial forces induced throughout the curved element because of the tangential component are also not of significant importance in the elastic analysis of the element, unlike plastic analysis. Therefore, it can be said that the bending moment in the middle of the curved element is induced merely by the tensile force's radial component.

Fig. 7 The quarter-ring device considered as a curved element with two fixed supports subjected to the concentrated tensile force *F* applied in the 45° direction
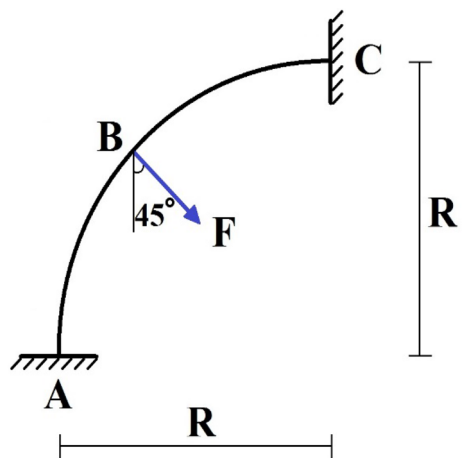
Fig. 8 Equivalent curved half-element
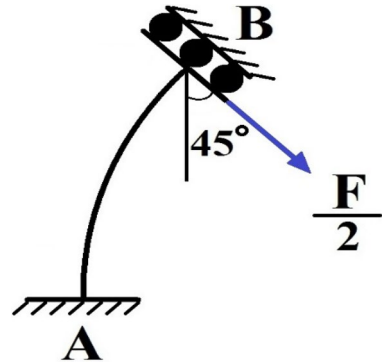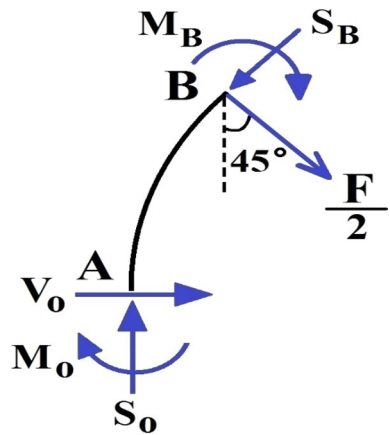

Fig. 9 Free body diagram of the equivalent curved half-element

As the geometry and loading of the abovementioned curved element are symmetrical, it can be replaced with an equivalent curved half-element, as illustrated in Fig. 8, which allows for easier analysis.

The equivalent half-element illustrated in Fig. 8 is a hyperstatic structure that cannot be analyzed using ordinary static equations. Given the support conditions, this structure has two redundancies making it two degrees indeterminate. Considering the free-body diagram shown in Fig. 9, where the bending moment and shearing force in the fixed support are denoted respectively as M_0 and V_0, the axial force in the fixed support, S_O, could be calculated using an equilibrium equation in the direction of the applied oblique force $F/2$ as follows:

$$\Sigma F = 0$$

$$\rightarrow S_0 \cos 45 - V_0 \cos 45 = \frac{F}{2} \rightarrow \frac{\sqrt{2}}{2}\left(S_0 - V_0\right) = \frac{F}{2} \rightarrow S_0 = \frac{\sqrt{2}}{2}F + V_0 \quad (1)$$

As shown in Fig. 10, the bending moment at the arbitrary node D chosen along the curved half-element could be specified based on the angle between radii connecting this node and node A to the origin O, denoted with θ, as $M(\theta)$. Accordingly, the bending moment $M(\theta)$ could be calculated by writing the equation for the equilibrium of moments about the arbitrary node D as follows:

$$
\begin{aligned}
\Sigma M &= 0 \\
\rightarrow M(\theta) &- V_0 R \sin\theta + S_0 R(1 - \cos\theta) + M_0 = 0 \\
\rightarrow M(\theta) &= -M_0 + V_0 R \sin\theta - S_0 R(1 - \cos\theta) \\
&= -M_0 + V_0 R \sin\theta - \left(\frac{\sqrt{2}}{2} F + V_0 \right) R(1 - \cos\theta) \\
&= -M_0 - V_0 R(1 - \sin\theta - \cos\theta) - \frac{\sqrt{2}}{2} FR(1 - \cos\theta)
\end{aligned}
\tag{2}
$$

Based on Eq. (2), the derivatives of $M(\theta)$ with respect to M_0 and V_0, needed in the next steps of the calculation, could be written as follows:

$$
\frac{\partial M(\theta)}{\partial M_0} = -1
\tag{3}
$$

$$
\frac{\partial M(\theta)}{\partial V_0} = -R(1 - \sin\theta - \cos\theta)
\tag{4}
$$

The total strain energy due to the flexural deformations in the half-element could be expressed with the following equation:

$$
U = \int_0^{\frac{\pi}{4}} \frac{M^2(\theta)}{2EI} R d\theta
\tag{5}
$$

where E is the modulus of elasticity of the yielding device's material, and I is the moment of inertia of the device about the bending axis (weak axis).

The virtual work method, along with the method of least work, are two of the well-known, powerful, and rigorous approaches in structural analysis by which several

Fig. 10 Free body diagram of the curved half-element for calculating $M(\theta)$
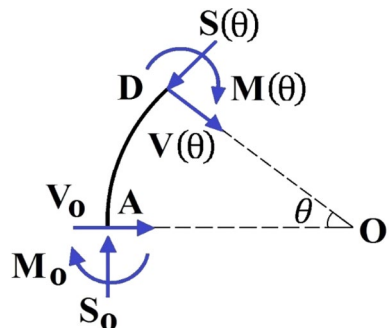
structural analysis problems related to the indeterminate systems have been addressed in previous studies (Fanaie et al. 2019; Fanaie and Tahriri 2017).

Based on the method of least work, the total strain energy should be minimized in terms of two independent parameters of M_0 and V_0. Using this method leads to the following equations:

$$\frac{\partial U}{\partial M_0} = 0 \rightarrow \frac{\partial}{\partial M_0}\left[\int_0^{\frac{\pi}{4}} \frac{M^2(\theta)}{2EI}Rd\theta\right] = 0 \rightarrow \int_0^{\frac{\pi}{4}} M(\theta)\frac{\partial M(\theta)}{\partial M_0}d\theta = 0$$

$$\rightarrow \int_0^{\frac{\pi}{4}} \left[-M_0 - V_0R(1 - \sin\theta - \cos\theta) - \frac{\sqrt{2}}{2}FR(1 - \cos\theta)\right] \times (-1) \times d\theta = 0$$

$$\rightarrow \left[-M_0\theta - V_0R(\theta + \cos\theta - \sin\theta) - \frac{\sqrt{2}}{2}FR(\theta - \sin\theta)\right]_0^{\frac{\pi}{4}} = 0$$

$$\rightarrow -M_0\frac{\pi}{4} - V_0R\left(\frac{\pi}{4}\right) - \frac{\sqrt{2}}{2}FR\left(\frac{\pi}{4} - \frac{\sqrt{2}}{2}\right) + V_0R = 0$$

$$\rightarrow \frac{\pi}{4}M_0 + V_0R\left(\frac{\pi}{4} - 1\right) = -\frac{\sqrt{2}}{2}FR\left(\frac{\pi}{4} - \frac{\sqrt{2}}{2}\right)$$

(6)

$$\frac{\partial U}{\partial V_0} = 0 \rightarrow \frac{\partial}{\partial V_0}\left[\int_0^{\frac{\pi}{4}} \frac{M^2(\theta)}{2EI}Rd\theta\right] = 0 \rightarrow \int_0^{\frac{\pi}{4}} M(\theta)\frac{\partial M(\theta)}{\partial V_0}d\theta = 0$$

$$\rightarrow \int_0^{\frac{\pi}{4}} \left[\begin{array}{c} -M_0 - V_0R(1 - \sin\theta - \cos\theta) \\ -\frac{\sqrt{2}}{2}FR(1 - \cos\theta) \end{array}\right] \times [-R(1 - \sin\theta - \cos\theta)]d\theta = 0 \quad (7)$$

$$\rightarrow \int_0^{\frac{\pi}{4}} \left[\begin{array}{c} M_0(1 - \sin\theta - \cos\theta) + V_0R(1 - \sin\theta - \cos\theta)^2 \\ +\frac{\sqrt{2}}{2}FR(1 - \cos\theta)(1 - \sin\theta - \cos\theta) \end{array}\right] d\theta = 0$$

To calculate the integral in Eq. (7), the following integrals need to be determined one by one:

$$\int_0^{\frac{\pi}{4}} (1 - \sin\theta - \cos\theta)d\theta = [\theta + \cos\theta - \sin\theta]_0^{\frac{\pi}{4}} = \frac{\pi}{4} - 1$$

(8)

$$\int_0^{\frac{\pi}{4}} (1 - \sin\theta - \cos\theta)^2 d\theta = \int_0^{\frac{\pi}{4}} \left(\begin{array}{c} 1 + \sin^2\theta + \cos^2\theta \\ -2\sin\theta - 2\cos\theta + 2\sin\theta\cos\theta \end{array} \right) d\theta$$

$$= \int_0^{\frac{\pi}{4}} (2 - 2\sin\theta - 2\cos\theta + \sin 2\theta) d\theta \tag{9}$$

$$= [2\theta + 2\cos\theta - 2\sin\theta - 0.5\cos 2\theta]_0^{\frac{\pi}{4}} = \frac{\pi - 3}{4}$$

$$\int_0^{\frac{\pi}{4}} (1 - \cos\theta)(1 - \sin\theta - \cos\theta) d\theta = \int_0^{\frac{\pi}{4}} \left(\begin{array}{c} 1 - \sin\theta - \cos\theta \\ -\cos\theta + \sin\theta\cos\theta + \cos^2\theta \end{array} \right) d\theta$$

$$= \int_0^{\frac{\pi}{4}} \left(1 - \sin\theta - 2\cos\theta + \frac{1}{2}\sin 2\theta + \frac{1 + \cos 2\theta}{2} \right) d\theta$$

$$= \int_0^{\frac{\pi}{4}} \left(\frac{3}{2} - \sin\theta - 2\cos\theta + \frac{1}{2}\sin 2\theta + \frac{1}{2}\cos 2\theta \right) d\theta \tag{10}$$

$$= [1.5\theta + \cos\theta - 2\sin\theta - 0.25\cos 2\theta + 0.25\sin 2\theta]_0^{\frac{\pi}{4}}$$

$$= \left(\frac{3\pi}{8} + \frac{\sqrt{2}}{2} - \sqrt{2} + \frac{1}{4} \right) - \left(1 - \frac{1}{4} \right) = \frac{3\pi}{8} - \frac{\sqrt{2}}{2} - \frac{1}{2}$$

By incorporating the integrals calculated in Eqs. (8), (9) and (10) into Eq. (7), the following equation is developed:

$$\left(\frac{\pi}{4} - 1 \right) M_0 + V_0 R \left(\frac{\pi - 3}{2} \right) + \frac{\sqrt{2}}{2} FR \left(\frac{3\pi}{8} - \frac{\sqrt{2}}{2} - \frac{1}{2} \right) = 0$$

$$\rightarrow \left(\frac{\pi}{4} - 1 \right) M_0 + V_0 R \left(\frac{\pi - 3}{2} \right) = -\frac{\sqrt{2}}{2} FR \left(\frac{3\pi}{8} - \frac{\sqrt{2}}{2} - \frac{1}{2} \right) \tag{11}$$

As observed, Eqs. (6) and (11) include two variables, namely M_0 and V_0, in terms of the external loading F and the radius R, which can be calculated by solving these equations. Accordingly, the bending moment, shearing force, and axial force of the fixed support shown in Fig. 9 can be expressed as follows:

$$M_0 = 0.0505 FR, \quad V_0 = 0.443 F, \quad S_0 = 1.15 F \tag{12}$$

Considering the Eq. (2) derived for the variable bending moment $M(\theta)$, the bending moment and compressive axial force at sliding support of B (corresponding to $\theta = 45°$, as depicted in Fig. 9), are defined by Eqs. (13) and (14), respectively:

$$M(\theta) = -M_0 - V_0R(1 - \sin\theta - \cos\theta) - \frac{\sqrt{2}}{2}FR(1 - \cos\theta)$$

$$M_0 = 0.0505FR, \quad V_0 = 0.443F$$

$$\rightarrow M_B = M(\theta = 45°) = -0.0505FR$$

$$-0.443FR\left(1 - \frac{\sqrt{2}}{2} - \frac{\sqrt{2}}{2}\right) - \frac{\sqrt{2}}{2}FR\left(1 - \frac{\sqrt{2}}{2}\right)$$

$$\rightarrow M_B = -0.0741FR$$

(13)

$$S(\theta = \cos 45°) = S_B, \quad \sum F = 0 \rightarrow S_B - V_0\cos 45° - S_0\cos 45° = 0$$

$$\rightarrow S_B = (S_0 + V_0)\cos 45° = (1.15F + 0.443F)\cos 45° = 1.126F$$

(14)

It can be concluded that the bending moment at node B is slightly more than that in the fixed support A. Hence, the first plastic hinge is expected to definitely form at the center of the yielding device, where the tensile cable force is exerted.

4 Design of the quarter-ring devices based on single plastic hinge formation criterion

The quarter-ring yielding devices in the proposed ring-cable-cylinder bracing system can be designed based on two approaches: the single plastic hinge formation criterion and the ultimate strength (capacity-based) method. This section presents the first approach, where the required thickness of each quarter-ring yielding device is determined based on the assumption that the connected cable's tensile force leads to the formation of a single plastic hinge at the point where it is exerted.

In the design process, it is assumed that quarter-ring devices are made of LYP steel with the uniaxial yield stress of F_y. In addition, the width of the curved devices, b, can be taken as that of beam flange (b_f) or higher values not exceeding 1.25 b_f. There are two other design parameters. The first one is the radius of the curved devices (R), which can be considered between 200 and 500 mm, and the second one is the thickness of the curved devices, t. Note that this thickness has to be limited to the minimum of the flange thickness values of the beam and column to which the ring is connected; otherwise, the use of stiffeners in the beam and column is obligatory. Considering that the force exerted on the quarter-ring and force components at its connection to the beam and column are tensile, the required strength of web and flange of beam and column under the forces applied by the quarter-ring can be determined and controlled and then the stiffener can be designed. When the required strength exceeds the available strength as determined considering the limit states of "Flange Local Bending" and "Web Local Yielding", stiffeners or doublers shall be provided and sized based on the difference between the required strength under the force S_o obtained from Eq. (12) and available strength based on the proposed limit states. The exact thickness value needs to be determined as presented in the following:

To determine the required thickness value, the tensile force applied to each yielding device by the bracing cable connected to them needs to be calculated. This tensile force, F_1, can be calculated by exposing the braced frame to the lateral force induced by an earthquake. This tensile force leads to a compressive axial force and a considerable bending moment in node B displayed in Fig. 7. While the compressive axial force is approximately

equal in nodes A and B, the bending moment is greater in node B. Therefore, node B is a critical point that needs to be controlled in determining the thickness of the yielding device. To do so, the following axial load-bending moment interaction equation can be implemented in this node:

$$\frac{M}{M_p} + \left(\frac{N}{N_y}\right)^2 = 1 \tag{15}$$

where M_p and N_y are the limit moment in pure bending (plastic bending moment) and the limit force in simple tension or compression (yield strength), respectively, defined as follows:

$$M_p = ZF_y = \frac{bt^2}{4}F_y, \quad N_y = AF_y = btF_y \tag{16}$$

where Z is the device's plastic section modulus (equal to $bt^2/4$ for rectangular sections), and A is the cross-sectional area of the quarter-ring device. Ultimately, the thickness of the curved device corresponding to the first plastic hinge force (F_1) is calculated utilizing the abovementioned interaction equation in the critical point B as in the following:

$$\frac{M}{M_p} + \left(\frac{N}{N_y}\right)^2 = 1, \quad M_B = -0.0741F_1R, \quad S_B = 1.126F_1$$

$$\rightarrow \frac{0.0741F_1R}{\frac{bt^2}{4}F_y} + \left(\frac{1.126F_1}{btF_y}\right)^2 = 1 \rightarrow \frac{F_1}{bt^2F_y}\left[4 \times 0.0741R + \frac{(1.126)^2F_1}{bF_y}\right] = 1$$

$$\rightarrow \frac{F_1}{bt^2F_y}\left[0.296R + \frac{1.268F_1}{bF_y}\right] = 1$$

$$\rightarrow t = \sqrt{\frac{F_1}{bF_y}\left[0.296R + \frac{1.268F_1}{bF_y}\right]} \tag{17}$$

5 Design of quarter-ring devices according to the ultimate strength (capacity-based) method

In this section, first, the practical and precise formulae to calculate the maximum strength of the quarter-ring devices, based on the formation of three plastic hinges in these curved elements and the internal work by axial forces, are derived via employing mathematical principles and the method of virtual work. Then, by equalizing the quarter-ring devices' obtained maximum strength with the cables' tensile yield strength (according to the capacity-based design method), the quarter-ring devices' required thickness is obtained.

Assuming that three bending plastic hinges are formed at the three nodes A, B, and C, and the middle node B undergoes an inward radial displacement equal to Δ, as shown in Fig. 11, the horizontal and vertical displacement components of node B will be equal to $\frac{\sqrt{2}}{2}\Delta$. The two arcs $\overarc{AB}$ and $\overarc{CB}$, which belong to the circle with the center O and the radius R, are expected to remain as arcs with radii the same as R subsequent to the plastic hinges' formation but with smaller angles—no longer equal to $\pi/4$. The assumption that these two new arcs, denoted by $\overarc{AB'}$ and $\overarc{CB'}$, remain as segments of circles with the radius R can be approximately correct if the bending and shearing deformations of the

Fig. 11 Deformation of the quarter-ring device under a 45° radial force
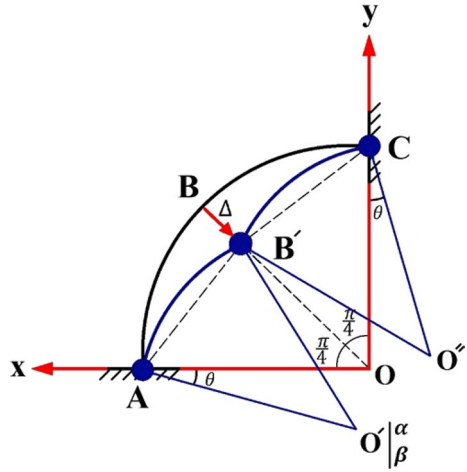
primary arcs under the displacement Δ are neglected, but this assumption needs to be modified at the end of this section. In such a case, the center of curvature for arcs $\overset{\frown}{AB'}$ and CB' will no longer be the point O and becomes O' and O'', respectively (Fig. 11).

The arcs $\overset{\frown}{AB}$ and CB experience a decrease in their length due to compressive axial forces as they deform into the arcs $\overset{\frown}{AB'}$ and CB'. To accurately tackle this problem without changing the $x - y$ coordinate system (the radius $\overline{OA}$ is the s-axis and the radius $\overline{OB}$ is the y-axis), the coordinates of new arcs' centers, i.e., points O' and O'', need to be calculated and utilized in the method of virtual work. Since the axial forces are approximately equal throughout the length of the primary arc, and the arcs $\overset{\frown}{AB}$ and CB' undergo the same reduction in the length due to the symmetry of the problem, the calculations can be focused on the arc $\overset{\frown}{AB}$, and the obtained results can then be extended to the arc CB as well, as presented in the following:

The equation of the initial circle in the $x - y$ coordinate system (before deformation) is as follows:

$$x^2 + y^2 = R^2 \tag{18}$$

If node B moves directly towards the center O as much as Δ, given that the radial extension $\overline{BB'}$ makes a 45° angle with each of the axes x and y, the coordinates of new point B's can be determined as:

$$x_{B'} = y_{B'} = (R - \Delta)\sin 45 = \frac{\sqrt{2}}{2}(R - \Delta) \tag{19}$$

If the point O' is considered as the center for the arc $\overset{\frown}{AB'}$ and it is assumed that the coordinates of this point are $O'^{\alpha}_{|\beta}$, as the center of a circle with the radius of R, the equation of arc $\overset{\frown}{AB'}$ can be expressed as Eq. (20):

$$\overset{\frown}{AB'} : (x - \alpha)^2 + (y - \beta)^2 = R^2 \tag{20}$$

Also, the coordinates of both points A and B' need to satisfy this equation:

$$A : \begin{cases} x_A = R \\ y_A = 0 \end{cases} \rightarrow (R - \alpha)^2 + (0 - \beta)^2 = R^2 \rightarrow R^2 - 2R\alpha + \alpha^2 + \beta^2 = R^2$$
$$\rightarrow \alpha^2 - 2R\alpha + \beta^2 = 0 \tag{21}$$

$$\rightarrow \alpha^2 + \beta^2 = 2R\alpha \tag{22}$$

$$B' : \begin{cases} x_{B'} = \frac{\sqrt{2}}{2}(R - \Delta) \\ y_{B'} = \frac{\sqrt{2}}{2}(R - \Delta) \end{cases} \rightarrow [\frac{\sqrt{2}}{2}(R - \Delta) - \alpha]^2 + [\frac{\sqrt{2}}{2}(R - \Delta) - \beta]^2 = R^2$$

$$\rightarrow \frac{1}{2}(R - \Delta)^2 - \sqrt{2}(R - \Delta)\alpha + \alpha^2 + \frac{1}{2}(R - \Delta)^2 - \sqrt{2}(R - \Delta)\beta + \beta^2 = R^2 \rightarrow \tag{23}$$

$$(R - \Delta)^2 - \sqrt{2}(R - \Delta)(\alpha + \beta) - R^2 + \alpha^2 + \beta^2 = 0 \rightarrow$$

$$R^2 - 2R\Delta + \Delta^2 - \sqrt{2}(R - \Delta)(\alpha + \beta) - R^2 + \alpha^2 + \beta^2 \rightarrow$$

$$\Delta^2 - 2R\Delta - \sqrt{2}(R - \Delta)(\alpha + \beta) + \alpha^2 + \beta^2 = 0$$

By replacing $\alpha^2 + \beta^2$ with $2R\alpha$ (obtained from Eq. (22)), Eq. (23) is redefined as follows:

$$\Delta^2 - 2R\Delta - \sqrt{2}(R - \Delta)(\alpha + \beta) + 2R\alpha = 0 \tag{24}$$

In the next steps, the values of α and β are first determined using Eqs. (21) and (24) in terms of radius R and displacement Δ, and then the coordinates of the center of the new circle, O', is calculated. For this purpose, the value of β is calculated in terms of R and α from Eq. (21) and then incorporated in Eq. (24):

$$\alpha^2 - 2R\alpha + \beta^2 = 0 \rightarrow \beta^2 = 2R\alpha - \alpha^2 \rightarrow \beta = -\sqrt{2R\alpha - \alpha^2} \tag{25}$$

$$\rightarrow \Delta^2 - 2R\Delta - \sqrt{2}(R - \Delta)\left(\alpha - \sqrt{2R\alpha - \alpha^2}\right) + 2R\alpha = 0$$

$$\rightarrow \Delta^2 - 2R\Delta - \sqrt{2}\alpha(R - \Delta) + \sqrt{4R\alpha - 2\alpha^2}(R - \Delta) + 2R\alpha = 0 \tag{26}$$

$$\rightarrow \Delta^2 - 2R\Delta - \sqrt{2}\alpha(R - \Delta) + 2R\alpha = -\sqrt{4R\alpha - 2\alpha^2}(R - \Delta)$$

Note that since the point O' is located under the x-axis, its vertical coordinate has a negative value.

Using Eq. (26), the value of α can be calculated in terms of the parameters R and Δ. In case of difficulty in solving Eq. (26) despite having R and Δ values, it is possible to estimate the approximate value of α through solving the following second-order equation in which the right-hand side is only a numerical value:

$$\sqrt{4R\alpha - 2\alpha^2} = \frac{2R\Delta}{R - \Delta} \tag{27}$$

Derivation of Eq. (27) based on Eq. (26) can be explained as follows:

After the formation of the three plastic hinges in the supports and the middle of the quarter-ring device (at the location of the tensile force from the cable), the middle plastic hinge B moves in the radial direction. At the beginning of the formation of the three plastic hinges, the middle plastic hinge's displacement Δ is a small amount, and

its squared value is much smaller, and therefore the first term of Eq. (26), Δ^2, can be neglected. The arc AC, whose center of curvature is node O, becomes the two arcs $\overset{\frown}{AB'}$ and $B'C$ as the plastic hinge B moves in the radial direction. The center of curvature of the arcs $\overset{\frown}{AB'}$ and $B'C$ are respectively the points O' and O''. Due to the small displacement of node B, the displacements of the centers of curvature of both arcs are also small relative to node O, and therefore the horizontal displacement of the center of curvature O' relative to the initial center of curvature O, assumed equal to α, is small. To eliminate the smaller terms and arrive at a simpler equation, if we omit the minimal term α^2 compared to the term $2R\alpha$ under the radical on the right side, the radical results in the term $\alpha^{0.5}$. Given that in numbers smaller than unity, smaller powers lead to larger values, it can be concluded that the third term $\sqrt{2}\alpha(R - \Delta)$ and the fourth term $2R\alpha$ on the left side of Eq. (26), which include α to the power of 1, are not decisive and can be ignored in the whole equation. Accordingly, Eq. (27) can be obtained by omitting the first, third, and fourth terms on the left of Eq. (26).

After determining the values of α and β, the central angle of the new arc, $\overset{\frown}{AO'B'}$, shown in Fig. 12, has to be calculated using trigonometry rules presented in Eq. (28). Using the value of this reduced angle (relative to 45°), γ, the reduction in the length of the arcs $\overset{\frown}{AB}$ and CB can be evaluated as presented in the following:

$$\frac{\left|\overline{AB'}\right|}{\sin\gamma} = \frac{R}{\sin\left(\frac{\pi}{2} - \frac{\gamma}{2}\right)} = \frac{R}{\cos\frac{\gamma}{2}} \rightarrow \frac{\sin\gamma}{\cos\frac{\gamma}{2}} = \frac{\left|\overline{AB'}\right|}{R}$$

$$\rightarrow \frac{2\sin\frac{\gamma}{2}\cos\frac{\gamma}{2}}{\cos\frac{\gamma}{2}} = 2\sin\frac{\gamma}{2} = \frac{\left|\overline{AB'}\right|}{R} \rightarrow \sin\frac{\gamma}{2} = \frac{\left|\overline{AB'}\right|}{2R} \tag{28}$$

The length of the arc $\overset{\frown}{AB'}$ is calculated as follows:

Fig. 12 Determining the angle AO′B′ using trigonometry rules
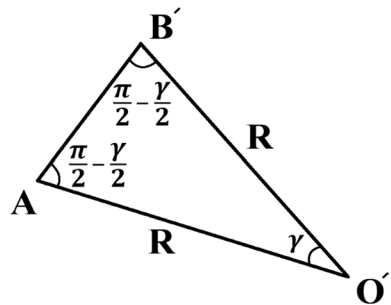
$$A \begin{bmatrix} x_A = R \\ y_A = 0 \end{bmatrix}, \quad B' \begin{bmatrix} x_{B'} = \frac{\sqrt{2}}{2}(R - \Delta) \\ y_{B'} = \frac{\sqrt{2}}{2}(R - \Delta) \end{bmatrix}$$

$$\rightarrow \left| \overline{AB'} \right| = \sqrt{\left[\frac{\sqrt{2}}{2}(R - \Delta) - R \right]^2 + \left[\frac{\sqrt{2}}{2}(R - \Delta) \right]^2} =$$

$$\sqrt{\frac{1}{2}(R - \Delta)^2 - \sqrt{2}R(R - \Delta) + R^2 + \frac{1}{2}(R - \Delta)^2} = \sqrt{(R - \Delta)^2 - \sqrt{2}R(R - \Delta) + R^2}$$

$$= \sqrt{\left(2 - \sqrt{2} \right)R^2 - \left(2 - \sqrt{2} \right)R\Delta + \Delta^2}$$

$$\simeq \sqrt{2 - \sqrt{2}} \times \sqrt{R^2 - R\Delta} \simeq \sqrt{2 - \sqrt{2}} \left(R - \frac{\Delta}{2} \right)$$

$$(29)$$

Equation (28) is rewritten as Eq. (30):

$$\sin \frac{\gamma}{2} = \frac{\left| \overline{AB'} \right|}{2R} = \frac{\sqrt{2 - \sqrt{2}} \left(R - \frac{\Delta}{2} \right)}{2R} = \sqrt{2 - \sqrt{2}} \left(\frac{1}{2} - \frac{\Delta}{4R} \right) \rightarrow$$

$$\frac{\gamma}{2} = \arcsin \left[\sqrt{2 - \sqrt{2}} \left(\frac{1}{2} - \frac{\Delta}{4R} \right) \right] \rightarrow \gamma = 2 \arcsin \left[\sqrt{2 - \sqrt{2}} \left(\frac{1}{2} - \frac{\Delta}{4R} \right) \right]$$

$$(30)$$

Ultimately, the reduction in the length of the arcs $\overset{\frown}{AB}$ and $\overset{\frown}{CB}$ are calculated using Eq. (31):

$$\Delta L_{AB} = \Delta L_{BC} = \Delta \gamma \times R = \left(\frac{\pi}{4} - \gamma \right) R = \left(\frac{\pi}{4} - 2 \arcsin \left[\sqrt{2 - \sqrt{2}} \left(\frac{1}{2} - \frac{\Delta}{4R} \right) \right] \right) R$$

$$(31)$$

Note that the answer obtained for the arcsine term in Eq. (31) must be converted into radians, then subtracted from $\frac{\pi}{4}$.

Utilizing the virtual work relationship to calculate sthe maximum radial load corresponding to the primary arc's mechanism (i.e., induced by the formation of three plastic hinges at fixed ends and middle of the arc as well as the internal work done by axial forces), requires the values of reduction in the length of the arcs $\overset{\frown}{AB}$ and CB obtained from Eq. (31). Considering that the axial force in the middle of the primary arc was determined to be equal to $S_B = 1.126F$ in the previous section, and assuming the rotation of plastic hinges at A and C supports equal to θ and the rotation of the plastic hinge at node B equal to 2θ, as illustrated in Fig. 13, the relationship between the internal and external work done in the quarter-ring device can be written as follows:

$$4M_P \times \theta + 2S_B \times \Delta L = F_2 \times \Delta \rightarrow 4M_P \times \theta + 2 \times 1.126F_2 \left(\frac{\pi}{4} - \gamma \right) R = F_2 \times \Delta \quad (32)$$

Note that although the axial force varies along the arcs $\overset{\frown}{AB}$ and $\overset{\frown}{CB}$, the variations are trivial. Therefore, by ignoring a small amount of error, the axial force at point B was used to write the virtual work relationship in Eq. (32). In this equation, F_2 is the device's ultimate strength equal to the maximum radial force applied to its center. More precisely, it is the radial component of the cable's tensile yielding force considered to

Fig. 13 Predicted deformed shape of the quarter-ring device after the formation of three plastic hinges
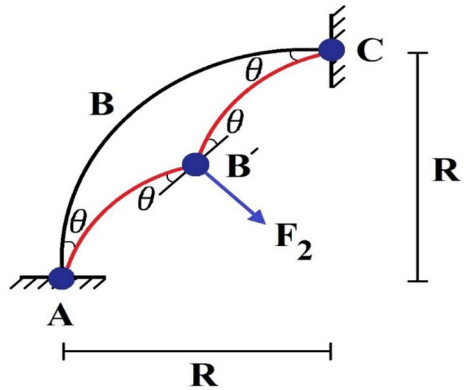
ensure each quarter-ring device and the cable connected to it simultaneously reach their ultimate capacity according to the capacity-based design method.

It should also be noted that although the force F_2 is considered to be equal to that of a radially connected cable, the cables, and thus their forces, in the proposed bracing system may not always be configured at a 45° direction, like those in the finite element model presented in Fig. 17b. In such a case, the virtual work relationship written as Eq. (32) is still applicable provided that the force F_2 is the radial component of the applied cable force. It is also worth mentioning that the tangential component of the cable force does not affect the virtual work relationship in Eq. (32). The reason is that the tangential component of the cable force is considered an anti-symmetrical loading for the device, and thus the amount of internal work done by it is equal to zero, as explained in the following. This anti-symmetrical tangential force leads to no bending moment in the middle of the device, its application point. Besides, despite the existence of clamping moments in the fixed supports, which are in the same direction, due to the opposite rotations of these supports (clockwise rotation of support A versus counter-clockwise rotation of support C), the virtual work related to such clamping moments neutralize each other as well. The anti-symmetrical tangential component of the cable force leads to a tensile force in one half of the arc and an equal compressive one in another half, which also neutralize the effects of each other when writing the second term in the left side of Eq. (32) (related to work done by axial force). Therefore, the tangential component of the cable force does not affect Eq. (32) at all. Thus, as stated before, if the cable force is not radially applied to the quarter-ring device, the only needed adjustment is to determine the radial component of the cable force and utilize it instead.

In what follows, the solution to the problem will be presented using two different highly accurate approximate methods.

5.1 Approximate solution 1

In this approximate solution, the rotation angle of plastic hinges in the fixed supports A and C (depicted in Fig. 11), i.e., θ, is considered to be equal to $\sin \theta$ since θ has a slight amount and this angle (in radians) can be replaced by $\sin \theta$:

$$\theta = \sin\theta = \frac{|y_{O'}|}{|\overline{O'A}|}, \quad y_{O'} = \beta = -\sqrt{2R\alpha - \alpha^2}, \quad |\overline{O'A}| = R$$

$$\to \theta = \sin\theta = \frac{\sqrt{2R\alpha - \alpha^2}}{R} \tag{33}$$

Thus, Eq. (32) is redefined as follows:

$$4M_P \times \frac{\sqrt{2R\alpha - \alpha^2}}{R} + 2.252F_2R\left(\frac{\pi}{4} - 2\arcsin[\sqrt{2 - \sqrt{2}}\left(\frac{1}{2} - \frac{\Delta}{4R}\right)\right] = F_2\Delta \tag{34}$$

As previously mentioned, in the presented calculations, the flexural and shearing deformations of the primary arc were ignored against the displacement Δ. Also, the secondary arcs $\overset{\frown}{AB'}$ and CB' were considered as circular arcs with the radius R, whereas, in reality, as shown Fig. 14, these arcs undergo plastic deformations and are no longer exactly circular.

Figure 14 shows the deformed shape of a steel quarter-ring with the geometric characteristics of $R = 500$ mm, $b = 150$ mm, and $t = 10$mm, modeled using Abaqus finite elements software. The modeling was done using second-order iso-parametric eight-noded quadrilateral thick shell elements with reduced integration (S8R), capable of considering shearing deformations in thick shell plates. It should be noted that reduced integration elements usually provide more accurate results and dramatically reduce analysis time, especially in three-dimensional models. The steel used in modeling was also considered to be mild steel with a yield stress of 240 MPa, the elastic modulus $E = 200,000$ MPa, and the Poisson's ratio $v = 0.3$. Besides, the two fixed supports in ends of the device were meled afully restrained. To improve the finite element modeling's accuracy, a small mesh size of 10 mm was chosen. The radial force applied to the center of the quarter-ring was also in the form of displacement control.

The results displayed in Fig. 14 indicate that the plastic deformation of the arcs $\overset{\frown}{AB'}$ and CB' has a minimal effect on the ΔL_{AB} and ΔL_{BC} values, but due to the significant amount of internal work carried out by axial forces in the device, these small changes in the lengths
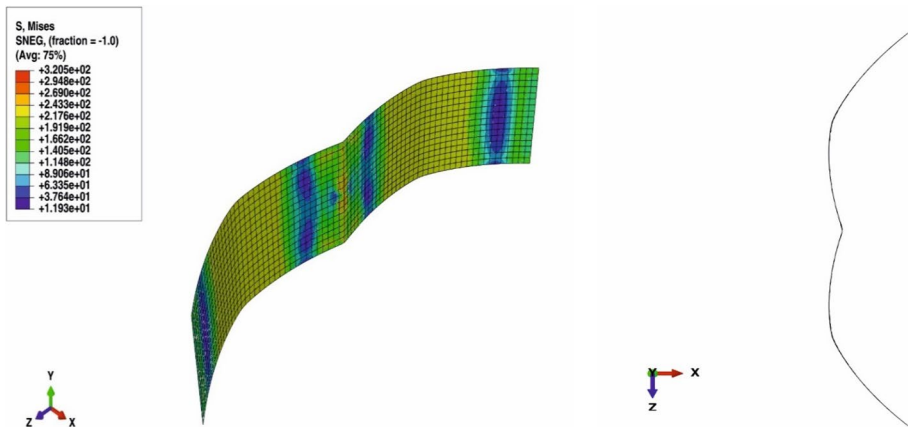

Fig. 14 Deformed shape of the FE model generated for the quarter-ring device ($R = 500$mm, $b = 150$mm., and $t = 10$mm) subjected to a 45° loading at its center

are not negligible (ΔL_{AB} and ΔL_{BC} were found to be less than expected). Moreover, the axial force's variable value along the curved device makes it difficult to determine the internal work done by this force. Therefore, to solve the problem, it is necessary to modify the work done by axial forces in the virtual work relationship with a reduction factor smaller than unity, denoted by X. To make this hypothesis and solution acceptable, it needs to be proved that X shows little change in various designs and can be considered as a constant factor in Eq. (35):

$$4M_P \times \frac{\sqrt{2R\alpha - \alpha^2}}{R} + 2.252F_2R\left(\frac{\pi}{4} - 2\arcsin\left[\sqrt{2 - \sqrt{2}}\left(\frac{1}{2} - \frac{\Delta}{4R}\right)\right]\right)X = F_2\Delta$$

(35)

The appropriate value of the reduction factor X lies between 0.65 and 0.7. This proposed factor is thoroughly examined and justified by implementing parametric analyses in Sect. 6. Also, note that to use Eq. (35), it is necessary to calculate the value of the central displacement Δ.

5.2 Approximate solution 2

In this approximate solution, although there is no need to calculate the values of α and β, answers are exceptionally accurate. In this procedure, the relationship between the rotation θ and the displacement of node B Δ, is expressed using the rigid body rotation law as follows:

$$\Delta_B = \Delta = \left|\overline{AB}\right| \times \theta = R\sin 45° \times \theta = \frac{\sqrt{2}}{2}R\theta \rightarrow \theta = \sqrt{2}\frac{\Delta}{R}$$

(36)

Utilizing Eqs. (36), (35) can be manipulated as follows:

$$4M_P \times \sqrt{2}\frac{\Delta}{R} + 2.252F_2R\left(\frac{\pi}{4} - 2\arcsin\left[\sqrt{2 - \sqrt{2}}\left(\frac{1}{2} - \frac{\Delta}{4R}\right)\right]\right)X = F_2\Delta$$

(37)

As previously recommended, thes appropriate value for the reduction factor X is in the range between 0.65 and 0.7. It is noteworthy that Eq. (37) is not dependent upon the amount of the displacement Δ. Thus, when designing a quarter-ring device, the thickness corresponding to the maximum strength can be simply obtained using this equation by choosing the values of R and b and selecting any desired value for Δ. However, the value of Δ must not be selected extremely large ($\Delta \not> 7.2R$), which leads to an acceptable argument for the arcsine term. The applicability and accuracy of Eqs. (17) and (37), are proved in Sect. 6 via drawing a comparison between analytical results and responses obtained using the developed formulae.

6 Finite element modeling of quarter-ring yielding devices in Abaqus

To confirm the accuracy of the proposed equations, considering a set of suggested ranges for the geometric parameters of the steel devices (R, b, and t), 36 finite element models made of mild steel with 240 MPa tensile yield strength were generated and analyzed in the Abaqus software with the specifications and the loading method as explained in the previous section. Figure 15 presents some of these generated models as examples.
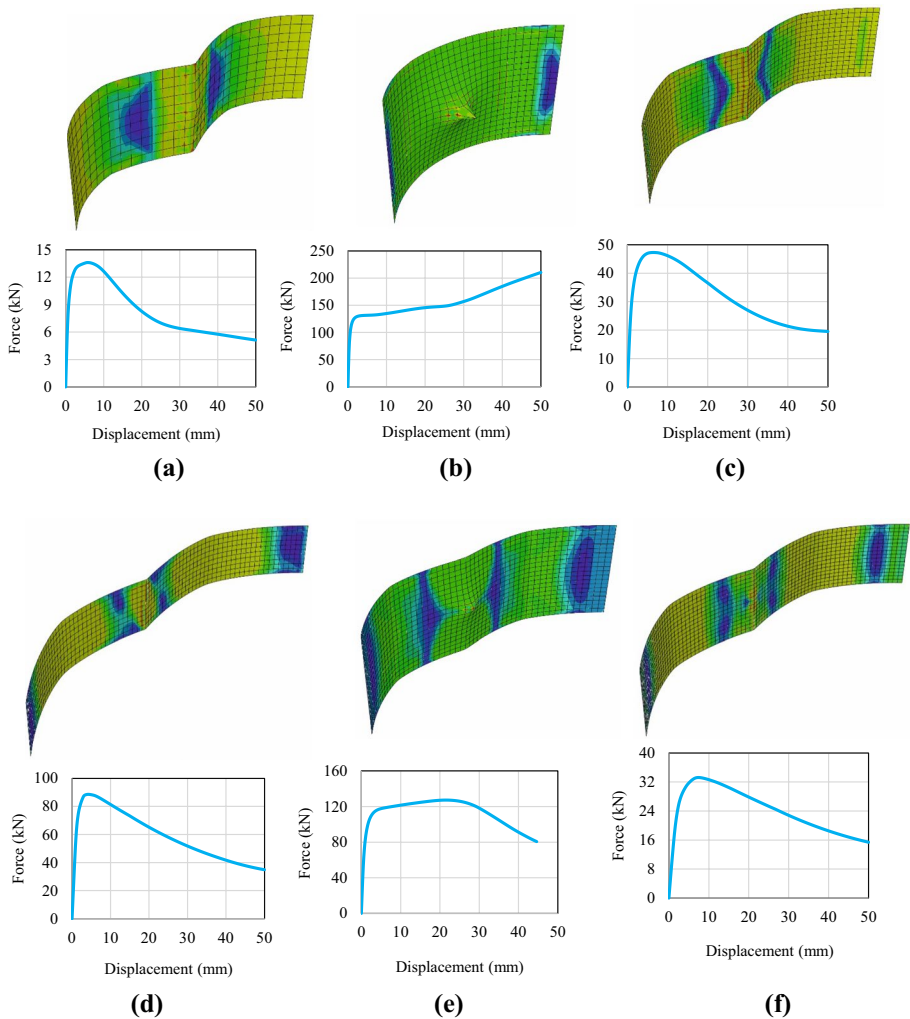
Fig. 15 FE models of quarter-ring devices subjected to loading at their center and their force–displacement diagrams **a** $R = 200$mm, $b = 100$mm, $t = 5$mm, **b** $R = 200$mm, $b = 200$mm, $t = 15$mm, **c** $R = 350$mm, $b = 150$mm, $t = 10$mm, **d** $R = 500$mm, $b = 100$mm, $t = 20$mm, **e** $R = 350$mm, $b = 200$mm, $t = 15$mm and **f** $R = 500$mm, $b = 150$mm., $t = 10$mm

The appropriate ranges for the geometric characteristics of the quarter-ring devices can be defined, based on dimensional features of steel IPE beams (connected to the devices) and the design suggestions recommended in previous sections, as in the following:

$$5 \text{ mm} \leq t \leq 20 \text{ mm}$$
$$200 \text{ mm} \leq R \leq 500 \text{ mm} \qquad (38)$$
$$100 \text{ mm} \leq b \leq 200 \text{ mm}$$

Table 1 reports the comparison between numerical results and the values obtained using Eqs. (17) and (37). Note that F_1 and F_2 forces were obtained from force–displacement

Table 1 Comparison between numerical results and those from the developed formulae

Model number	Radius of the Damper, R (mm)	Width of the Damper, b (mm)	Thickness of the Damper, t (mm)	F_1 (N)	F_2 (N)	Estimated thickness by Eq. (17) (mm)	Estimated thickness by Eq. (37) and X = 0.65 (mm)	$\frac{F_2(N)}{F_1(N)}$
1	200	100	5	10,062.7	13,597.4	5	5.62	1.35
2	200	100	10	41,719.5	51,835.1	10.33	10.96	1.24
3	200	100	15	94,000	109,797	15.85	15.95	1.17
4	200	100	20	163,000	181,230	21.46	20.54	1.11
5	200	150	5	12,400	24,474.9	4.5	6.17	1.97
6	200	150	10	50,000	85,743.6	9.2	11.56	1.71
7	200	150	15	112,000	148,883	14	15.25	1.33
8	200	150	20	195,000	221,340	18.91	18.57	1.135
9	200	200	5	12,100	40,971.9	3.9	6.93	3.39
10	200	200	10	52,000	127,161	8.1	12.25	2.44
11	200	200	15	126,000	210,598	12.8	15.75	1.67
12	200	200	20	205,000	299,433	16.6	18.8	1.46
13	350	100	5	6700	7604.48	5.38	5.58	1.13
14	350	100	10	28,000	32,825.6	11	11.57	1.17
15	350	100	15	61,425	72,013.2	16.5	17.1	1.17
16	350	100	20	105,000	122,681	21.85	22.33	1.16
17	350	150	5	8500	11,515.8	4.95	5.58	1.35
18	350	150	10	38,000	47,286.4	10.52	11.31	1.24
19	350	150	15	87,000	104,974	16	16.94	1.2
20	350	150	20	158,000	180,743	21.8	22	1.14
21	350	200	5	10,000	16,419.5	4.65	5.77	1.64
22	350	200	10	44,000	61,524.2	9.8	11.18	1.4
23	350	200	15	101,000	127,278	15	16	1.26
24	350	200	20	180,000	211,091	20.15	20.72	1.17
25	500	100	5	4254	4854.9	5.12	5.3	1.14
26	500	100	10	18,600	22,012.4	10.74	11.3	1.18

Table 1 (continued)

Model number	Radius of the Damper, R (mm)	Width of the Damper, b (mm)	Thickness of the Damper, t (mm)	F_1 (N)	F_2 (N)	Estimated thickness by Eq. (17) (mm)	Estimated thickness by Eq. (37) and X = 0.65 (mm)	$\frac{F_2(N)}{F_1(N)}$
27	500	100	15	42,000	50,913.8	16.21	17.21	1.21
28	500	100	20	70,000	88,627.4	21	22.7	1.26
29	500	150	5	5850	7429.6	4.91	5.36	1.27
30	500	150	10	26,000	33,232.7	10.37	11.34	1.28
31	500	150	15	61,000	76,972.9	15.95	17.3	1.26
32	500	150	20	110,000	134,267	21.54	22.8	1.22
33	500	200	5	7050	10,207.8	4.66	5.43	1.45
34	500	200	10	34,500	43,881	10.34	11.28	1.27
35	500	200	15	75,000	100,133	15.31	17	1.33
36	500	200	20	136,000	176,366	20.72	22.86	1.29

diagrams of the quarter-ring device models. As observed in this table, both Eqs. (17) and (37) with the reduction factor $X = 0.65$, were capable of accurately predicting the thickness of the 36 modeled devices with low percentage error and close approximation. In addition, the obtained results demonstrate that by keeping the ultimate strength, i.e., the radial force F_2 value, constant in two of the distinct models reported in Table 1 (for example, case 2 and 27, or case 16 and 23), a reduction in devices' radius R and an increase in devices' width b, lead to a decrease in the required thickness. For further assurance, the calculated thickness can be rounded to a greater value.

The main reason for the different plastic mechanisms observed in Fig. 15b and e can be explained according to Saint–Venant's principle. Based on this principle, whenever a load is applied at a given section, the stress distribution at a section at a distance equal to or greater than the member's width is uniform. In other words, except in the vicinity of load application points, the stress distribution can be assumed to be independent of the actual mode of load application. This assumption is valid not only for axial loading but also for virtually any type of loading. Therefore, according to Saint–Venant's principle, if the dampers' width is increased, an almost uniform stress distribution will occur at a distance further away from the load application point, and there will be a more significant difference between this uniform stress distribution and the stress distribution at the vicinity of load application area. Furthermore, according to Table 1, it can be said that smaller values of F_2 to F_1 ratio lead to shorter intervals between the formation of the first plastic hinge and the complete spread of plasticity across the quarter-ring device, and hence, it has a rapid distributed plasticity mode instead of concentrated plasticity. Also, smaller F_2 to F_1 ratios lead to a rapid formation of resistance in the whole quarter-ring device against the applied central load. From the recurring trend of the value of F_2 to F_1 ratio in Table 1, it can be concluded that decreased thickness, decreased radius, and increased width of the quarter-ring lead to the increase of this ratio, resulting in a concentrated plasticity mode instead of a distributed plasticity mode. It should be noted that according to Fig. 15, the occurrence of concentrated plasticity is much more desirable than a rapid distributed plasticity mode in the quarter-ring devices. More precisely, if the dampers are to be designed to increase energy dissipation in the frame, the area under the force–displacement graph must be maximized for a given load. The reason for this is that in this special geometric case of quarter-ring dampers, the spread of forces and consequently plasticity in the quarter-ring is more difficult, and the given damper needs a much larger central displacement at a constant force to be able to extend plasticity all along its length. This larger displacement at a constant force causes greater ductility and energy dissipation in the damper and the whole steel frame.

It should be noted that because the formulae presented in this study are also based on distributed plasticity and uniform deformation along the quarter-ring devices, their accuracy in the case of concentrated plasticity is slightly lower. However, the answers provided (especially in the case of the formation of three plastic hinges at ultimate strength) are highly acceptable.

It should be added that the accuracy of Eqs. (37) and (17) was also verified for LYP100 and ST44 steel types and different geometrical properties than those provided in Table 1, but to avoid excessive redundancy, they are not included herein.

7 Finite element modeling of a portal moment frame equipped with the proposed ring-cable-cylinder bracing system

To investigate the effects of utilizing quarter-ring yielding devices on the performance of the ordinary cable-cylinder bracing system, first, the portal moment frame tested by Hou and Tagawa (2009) was meticulously modeled and verified using the Abaqus finite element software. Subsequently, four quarter-ring yielding devices, designed based on the frame's characteristics, were added to this system, and the performance of the resulting ring-cable-cylinder bracing system was compared with that of the ordinary cable-cylinder bracing system.

As illustrated in Fig. 16, the original frame examined by Hou and Tagawa (2009) had similar beam and column sections of H-150×150×7×10, with T-stub connections of H-300×150×6.5×9 made from SS400 steel. The bracing members in this system are stainless steel (SUS316) strand (7×19) cables passing through a steel pipe (high-stiffness pipe) with the length, inner diameter, and thickness of 214, 40, and 15 mm, respectively. The geometric dimensions of this steel pipe were calculated based on the drift at which the cables start functioning, considered equal to 30 mm. Also, the tensile force corresponding to cables' yielding was reported to be approximately equal to 58 kNin this sub-assembly.

Given the difference of lower than 10 degrees between the cable direction and radial direction of the devices (cos $10^{\circ} \simeq 1$), using Eq. (37) with $X = 0.65$ and $F_2 = 58$ kN the minimum required thickness of the modeled devices was estimated to be 15 mm. Each device's
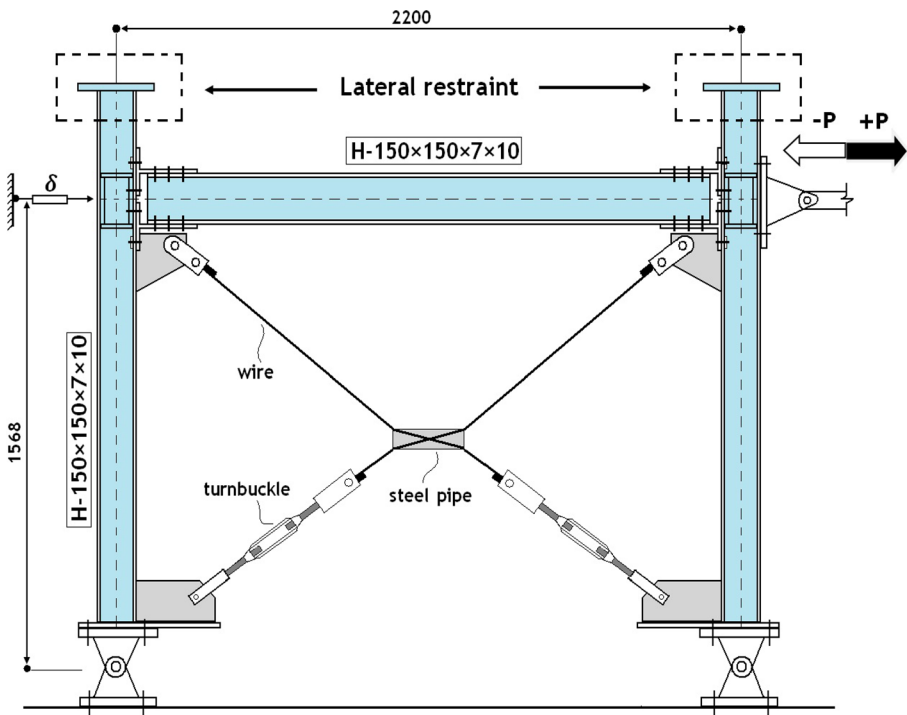

Fig. 16 The portal moment frame sussembly with a cable-cylinder bracing system tested by Hou and Tagawa (2009)

radius and width were also considered to be 300 mm and 200 mm, respectively. LYP steel with the yielding stress of about 100 MPa and $E=200,000$ MPa was also used as devices' material.

The finite element models were generated considering all of the continuity and doubler plates, column stiffeners, gusset plates, and base plates used in the previously tested experimental frame (Fig. 17). The thickness of baseplates was determined so that they provide enough stiffness and lead to full plastification of the connected quarter-ring devices during cyclic loading. The out-of-plane displacement of the modeled frame was also restricted at the top of the columns. Besides, both supports in the models were considered as the pinned type. As beam and columns are meant to remain elastic during the loading, their material properties were considered as perfectly elastic in the modeling procedure. The cables were modeled using the wire element with the beam section, and the central steel pipe was considered as a rigid shell cylinder. The modeling of other members was done using
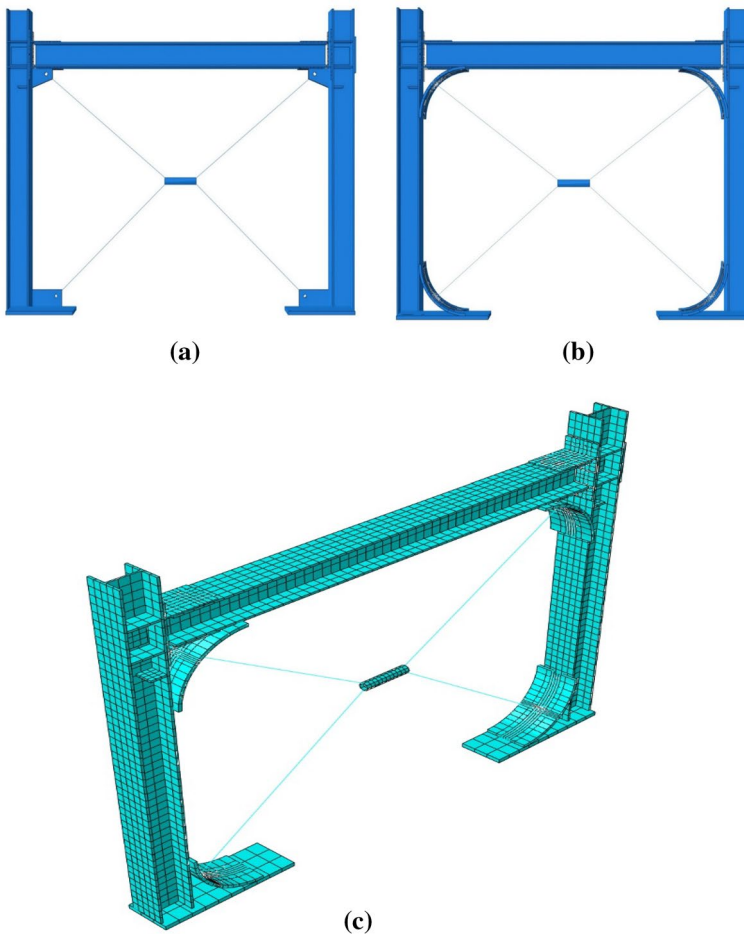

(a)   **(b)**

(c)

Fig. 17 FE modeling **a** portal moment frame with the cable-cylinder bracing system tested by Hou and Tagawa (2009) **b** the proposed system equipped with curved quarter-ring yielding devices **c** an example of a meshed FE model

Fig. 18 The displacement-controlled loading protocol applied to the experimental specimen (Hou and Tagawa 2009) and the finite element models
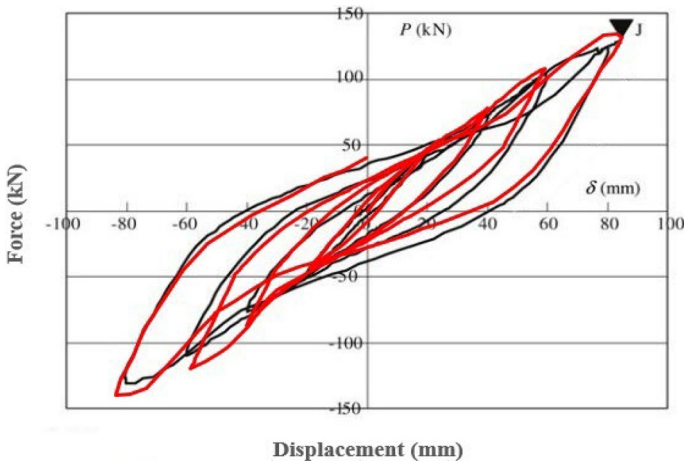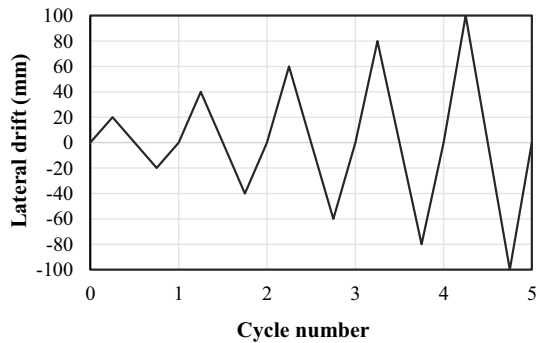

Fig. 19 Verification of the hysteresis behavior of the modeled cable-cylinder bracing system

solid elements. To enhance the accuracy of the modeling responses, the C3D2OR element, which is an excellent general-purpose element and rarely exhibits hour-glassing despite the reduced integration, was utilized for T-stubs and the yielding quarter-ring devices.

Note that to avoid the problems related to the convergence of the results, frictionless surface interaction was employed for the T-stub connections. Furthermore, as shown in Fig. 18, the cyclic loading applied to the top of finite element models was a displacement-controlled loading protocol, fully consistent with the one implemented in the experiment done by Hou and Tagawa (2009).

In the experiment done by Hou and Tagawa (2009), the cables were ruptured in the lateral drift of 80 mm, and then the experiment was stopped. The verification of the finite element modeling conducted in the present study is presented in Fig. 19. As can be seen, the finite element model shows a high level of precision and agreement with the laboratory test results.

Figure 20 presents the improvement in the ordinary cable-cylinder bracing system's cyclic behavior after the addition of quarter-ring yielding devices. Figure 21 also depicts the backbone curves obtained for the models analyzed. Besides, Figs. 22 and 23 show the deformed shape of the ring-cable-cylinder frame after the cyclic loading in terms of
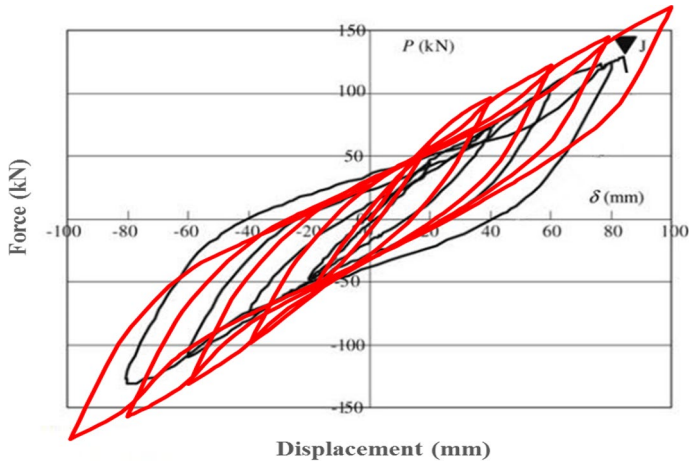
Fig. 20 Comparison of hysteresis behavior between the ordinary cable-cylinder bracing system examined by Hou and Tagawa and the proposed system
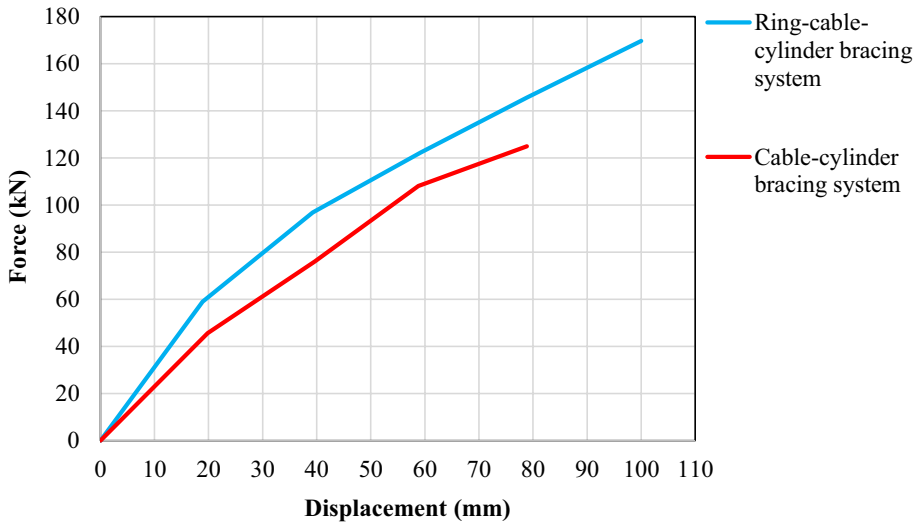

Fig. 21 Comparison of backbone curves in the ring-cable-cylinder system and the cable-cylinder bracing system experimented by Hou and Tagawa (2009)

S-Mises stress and AC-Yield failure contours, respectively. Regarding the results obtained for the frames modeled with and without quarter-ring yielding devices, it can be concluded that utilizing these proposed devices is an efficient modification which dramatically enhances the behavior of the cable-cylinder bracing system. While the quarter-ring system and the cable-cylinder system are systems in series with less equivalent stiffness than those of each of the two separate systems, the quarter-ring devices, especially the upper ones, significantly increase the stiffness of the moment frame system under cyclic loading. This
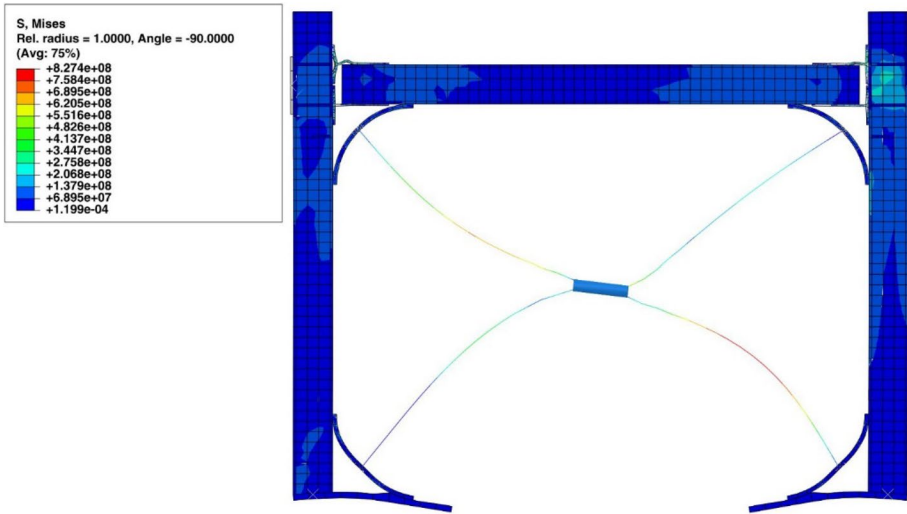
Fig. 22 Deformed shape of the ring-cable-cylinder frame after the cyclic loading in terms of S-Mises stress contour
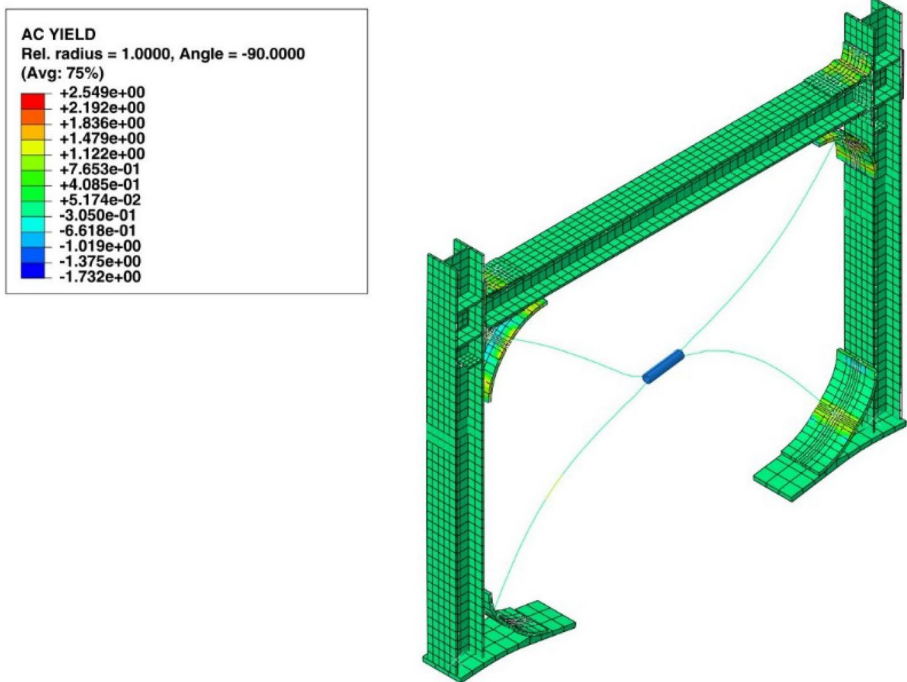

Fig. 23 Deformed shape of the ring-cable-cylinder frame after the cyclic loading in terms of AC-Yield stress contour

Table 2 Comparison of the proposed system with the conventional cable-cylinder bracing system

Systems' ratio	Ultimate strength (kN), ratio	Initial stiffness (kN/m), ratio	Dissipated energy (kJ), ratio	Ductility ratio
New system/Conventional system	$\frac{169.69}{124.16} = 1.37$	$\frac{3122.28}{2302.07} = 1.36$	$\frac{57.18}{24.84} = 2.3$	$\frac{5.29}{4.03} = 1.31$

increase in stiffness can compensate for the decreased equivalent stiffness attributed to utilizing the two systems in series and improve the whole frame's stiffness. More precisely, the overall structural system's stiffness is affected by the interaction of three stiffness components attributed to the bare moment frame, quarter-ring devices, and the cable-cylinder bracing. Utilizing quarter-ring devices leads to decreased stiffness when used in series with the cable-cylinder bracing system but increased stiffness when incorporated into the bare frame system in such a way that the increase in stiffness is more significant than the decrease and neutralizes it. The reason for the increase in the bare moment frame's stiffness is that the quarter-ring devices reduce the relative rotation angle of the beams and columns, which ultimately significantly increases the rotational stiffness of the beam-to-column connections and reduces the story drift angle.

The results presented in Table 2 also demonstrate that the proposed yielding devices improved the performance of the cable-cylinder bracing system with a 37% increase in ultimate strength, a 36% increase in initial stiffness, a 31% increase in ductility (the ratio of ultimate displacement to the initial yield displacement), and a remarkable 130% increase in energy dissipation. The simultaneous increase of stiffness, strength, and energy dissipation (by an exceptional amount) can be reckoned as one of the special merits of the proposed system since the stiffness and energy dissipation are usually inversely proportionate. It can also be concluded that the addition of quarter-ring devices made of LYP steel significantly alleviated the effects of pinching behavior observed in the experiment (shown in Fig. 20). An increase in the system's tolerable drift from 80 mm to 100 mm, prevention of the rupture of the cables connected to the beam-to-column connections because of the early yielding of the quarter-ring devices, and finally, the improvement of the overall performance level of the system can be named as other advantages observed.

8 Conclusions

In the current study, an innovative cable-cylinder bracing system equipped with quarter-ring curved yielding devices was introduced. This system, termed the ring-cable-cylinder system, exhibits excellent energy dissipation and ductility and also leads to simultaneous improvements in the frame's stiffness and strength characteristics. Based on least and virtual work methods, a set of equations and design recommendations were presented for the design of the proposed quarter-ring devices which are able to compute their thickness in two distinct failure mechanism cases: (i) the initial formation of a single flexural plastic hinge; (ii) the subsequent formation of three plastic hinge at ultimate strength. The accuracy of the proposed equations was assessed by performing 36 FE analyses. In the final part of the paper, the performance of a verified steel moment frame model equipped with the proposed bracing system was evaluated under cyclic loading. The most significant results of this study can be outlined as in the following:

1. The proposed ring-cable-cylinder bracing system with quarter-ring yielding devices can be easily implemented at a low cost in steel frames vulnerable to lateral forces. This system is very flexible and can be easily replaced after a severe earthquake if other elements would remain intact.
2. The proposed system can prevent severe damage to beam-to-column connections by concentrating it in the quarter-ring devices and postpone the bracing system's failure through early yielding of the quarter-ring devices made of low-yield-point steel.
3. The arch action in the quarter-ring devices and the utilization of low-yield-point steel lead to a decrease in the occurrence of local buckling, reduced compactness ratio, and an increase in the system's long-term cyclic stability.
4. The presented equations allow for a reliable estimation of the required thickness of the quarter-ring devices in the two failure mechanism cases of single flexural plastic hinge formation and three plastic hinges formation at ultimate strength, respectively. They do not depend on the middle radial displacement of the ring. It is recommended that the device width should not exceed 1.25 times the smallest value of beam and column flange width. Moreover, the device radius should be considered in the range of 200 to 500 mm.
5. The parametric analysis conducted indicated that for a constant ultimate strength of the devices, which corresponds to the cables' yield strength, both the reduction in the radius and the increase in width of the quarter-ring devices lead to the decrease in required thickness.
6. The addition of the yielding devices to the cable-cylinder bracing system in the steel moment frame tested by Hou and Tagawa (2009) resulted in a 36% gain in initial stiffness, a 37% increase in ultimate strength, a 31% gain in ductility, and a noticeable 130% increase in energy dissipation together with a notable reduction of adverse pinching effects.

In the end, it must be noted that in numerical modeling performed in the Abaqus software presented in this study, the behavior of steel materials was modeled as elastic-perfectly plastic, and the strain-hardening in steel materials was not considered. Considering the strain-hardening behavior of steel used as quarter-ring dampers' material is an exciting research topic that demands further investigations and distinct insight into the derivation of the quarter-ring thickness; however, the volume of such a research work would not fit into the current paper and can be presented in future studies. This research can be undertaken by first deriving new relationships between ultimate bending moment strength (M_u) and plastic bending moment (M_P) of the steel used to fabricate the quarter-ring devices. Then, new relationships for the internal work done by axial forces along the quarter-ring with regard to axial hardening of the steel can be obtained. In the final stage, finite element simulation can be utilized to verify the proposed formulae and the initial assumptions.

It should also be noted that while the consideration of the quarter-ring devices' connections to the corresponding frame as rigid connections in the presented calculations is an acceptable assumption according to the numerical analyses performed in this study, the optimum design and behavior analysis of these connections requires a comprehensive investigation, which can be another interesting research topic for future studies.

Declarations

Conflict of interest The authors have no relevant financial and non-financial interests to disclose.

Informed consent All authors named on the submission of this paper, made significant contributions throughout the preparation of the work and agree to be accountable for all aspects of the work, and also will be fully responsible to any obscure part mentioned by revered peer reviewers.

References

Andalib Z, Kafi MA, Kheyroddin A, Bazzaz M (2014) Experimental investigation of the ductility and performance of steel rings constructed from plates. J Constr Steel Res 103:77–88

Beheshti-Aval SB, Mahbanouei H, Zareian F (2013) A hybrid friction-yielding damper to equip concentrically braced steel frames. Int J Steel Struct 13:577–587

Chen SJ, Jhang C (2011) Experimental study of low-yield-point steel plate shear wall under in-plane load. J Constr Steel Res 67(6):977–985

Chen Y, Chen C, Jiang H, Liu T, Wan Z (2019) Study of an innovative graded yield metal damper. J Constr Steel Res 160:240–254

Chen SC, Zheng LY, Yan WM, Kim K-S (2020) Seismic performance of post-tensioned precast concrete joints improved with curved steel braces. J Earthq Eng: 1–19

Cheraghi A, Zahrai SM (2017) Cyclic testing of multilevel pipe in pipe damper. J Earthquake Eng 23:1695–1718

Deng K, Pan P, Wang C (2013) Development of crawler steel damper for bridges. J Constr Steel Res 85:140–150

Fanaie N, Tahriri M (2017) Stability and stiffness analysis of a steel frame with an oblique beam using method of least work. J Constr Steel Res 137:342–357

Fanaie N, Aghajani S, Afsar Dizaj E (2016) Strengthening of moment-resisting frame using cable–cylinder bracing. Adv Struct Eng 19:1736–1754

Fanaie N, Faegh SS, Partovi F (2019) An improved and innovative formulation for calculating amplified elastic story drift induced by RBS connections in steel moment frames. J Constr Steel Res 160:510–527

Henriques J, Calado L, Castiglioni CA, Degée H (2019) Dissipative connections with U-shaped steel plate for braces of concentrically braced frames. Bull Earthq Eng 17:6203–6237

Hou X, Tagawa H (2009) Displacement-restraint bracing for seismic retrofit of steel moment frames. J Constr Steel Res 65:1096–1104

Hsu HL, Halim H (2017) Improving seismic performance of framed structures with steel curved dampers. Eng Struct 130:99–111

Maleki S, Mahjoubi S (2013) Dual-pipe damper. J Constr Steel Res 85:81–91

Taiyari F, Mazzolani FM, Bagheri S (2019) A proposal for energy dissipative braces with U-shaped steel strips. J Constr Steel Res 154:110–122

Utomo J, Moestopo M, Surahman A, Kusumastuti D (2015) Estimating the ultimate energy dissipation capacity of steel pipe dampers. Proc Eng 125:1101–1107

Xie X, Chen SX, Zhou X (2018) A simplified analytical model for U-shaped steel dampers considering horizontal bidirectional deformation. Bull Earthq Eng 16:6243–6268

Zahrai SM, Hosein Mortezagholi M (2017) Cyclic performance of an elliptical-shaped damper with shear diaphragms in chevron braced steel frames. J Earthquake Eng 22:1209–1232

Zhang C, Aoki T, Zhang Q, Wu M (2013) Experimental investigation on the low-yield-strength steel shear panel damper under different loading. J Constr Steel Res 84:105–113

Publisher's Note Springer Nature remains neutral with regard to jurisdictional claims in published maps and institutional affiliations.